Egypt. J. Chem. **Vol. 65,** No. 10 pp. 119 - 129 (2022)

Egyptian Journal of Chemistry

http://ejchem.journals.ekb.eg/

Preparation and Characterization of ZnO Thin Film on Anodic Al_2O_3 As A Substrate for Several Applications

E. M. Elsayed [a] Ashraf K. Eessaa [b], M. M. Rashad [c], and Ashraf M. El-Shamy [d,*]

[a] *Central Metallurgical Research and Development Institute (CMRDI), Chemical and Electroprocessing Department P.O. BOX.87 Helwan, Egypt11421*

[b] *Electronic Research Institute (ERI), Nanotechnology lab, Dokki., Cairo, Egypt*

[c] *Central Metallurgical Research and Development Institute (CMRDI), Electronic and Magnetic Materials Department P.O. BOX.87 Helwan, Egypt11421*

[d] *National Research Centre, Physical Chemistry Department, Electrochemistry and Corrosion Lab., El-Bohouth St. 33, Dokki, P.O. 12622, Giza*

Abstract

A unique approach for customizing nanowire zinc oxide thin films on nanoporous anodic Al_2O_3 (nPAA) was developed in this study, which included the use of an electrochemical procedure to manufacture nanowire zinc oxide thin films on nanoporous anodic Al_2O_3 (nPAA). With a single step of anodization at 25 ^oC and low voltage, we were able to produce a conventional nPAA template. The embedding of ZnO arrays in nPAA pores was a subsequent step in the process of creating the device. During the electrodeposition process, the techniques of cyclic voltammetry, linear sweep voltammetry, and chronoamperometry were used to determine whether zinc oxide was being electrode deposited on the nPAA. The results of these measurements were compared to the results of the other measurements. For the investigation of ZnO/nPAA assemblies, field emission scanning electron microscopy (FE-SEM) and dispersive X-ray spectroscopy (DXS) was used to determine the morphological structures and chemical compositions of the assemblies, as well as to determine their mechanical and electrical properties (EDX). Several developing sectors have the potential to profit from the materials that have been discovered so far, including electronics, battery energy storage, and photocatalysis.

Keywords: *Electrodeposition;* ZnO Nanocomposite; Anodic Aluminum Oxide; Chronoamperometry; Surface Characterization.

1. Introduction

In addition to molten salt separation and catalysis, nanoporous anodic aluminum oxide (nPAA) has several applications in electronics, photonics (including sensing and drug administration), photonics (including sensing and drug administration), and template creation, to mention a few [1,2]. Anodization of aluminum is a straightforward, low-cost method that produces nanoporous structures that are vertically aligned and highly organized [3,4].

Using this method, nanoporous constructs may be created and used in a variety of applications [5,6]. Different characteristics of nPAA may be seen in terms of its chemical, optical, mechanical, and electrical properties. Hardness, chemical resistance, biocompatibility, thermal stability, and a substantial quantity of exterior space are some of the characteristics of this material. Because of its exceptional photosensitive and electrochemical capabilities, nanoporous nPAA has been extensively researched as a platform for developing low-cost applications [7,8].

The anodization of the Al_2O_3 membrane acts as a superb template to produce highly organized nanowire clusters, and it is effective [9,10]. A self-organized process that occurs during the anodization of aluminum in acidic media has emerged over the past few years as one of the most important and extensively utilized methods for the generation of highly planned nanowires [11,12]. ZnO is regarded to be one of the most promising oxide semiconductor materials due to its exceptional optical, electrical, and piezoelectrical capabilities [13,14].

The construction of appropriately designed nanowire collections is a vital milestone in the development of micro-optoelectronic devices [15,16]. In the past, ordered ZnO nanowire arrays implanted in AAM templates have been created by electrodepositing Zn into AAM nanopores to form metallic nanowire arrays and then oxidizing them, and

*Corresponding author e-mail: am.elshamy@nrc.sci.eg; elshamy10@yahoo.com.

Receive Date: 09 December 2021, Revise Date: 21 July 2022, Accept Date: 23 February 2022

DOI: 10.21608/EJCHEM.2022.110382.5021

these arrays have been demonstrated to be successful in a variety of applications [17,18]. While the method's applicability is limited by the considerable period (about 35 hours) required for thermal oxidation at 300 ^{o}C, its application is not achievable [19,20].

A unique technique has been established for the creation of the zinc oxide film, which has now been used in the development of the CdO film as well [21,22]. This technology has also been applied to the preparation of the CdO film. DMSO solution containing zinc chloride and a molecular oxygen precursor was used to fabricate ZnO nanowire arrays [23,24]. A DMSO solution containing zinc chloride and a molecular oxygen precursor was used to create ZnO nanowire arrays, which were then studied [25,26]. ZnO nanowire arrays that have been put in an AAM template have been studied in terms of their morphological structures and photoluminescence capabilities by researchers [27,28].

The use of non-aqueous baths enables the use of greater deposition temperatures since they do not dissolve in water [29,30]. We have been able to characterize the material produced using an electrodeposition manufacturing technique of zinc oxide nanowire on nonporous anodic alumina templates (nPAA) and factors affecting nonporous anodic alumina templates (nPAA) [31,32]. The influence of electrolyte content (H_3PO_4 acid) and anodizing period on the morphology of nPAA produced will be examined in this work, which will use the chronoamperometric approach [33,34]. Scanning electron microscopy (SEM) will be used to analyze the morphology of the nPAA [35,36]. Here, we will look at the impact of several factors on the morphology of the ZnO films that have been formed, including bath agitation, anodization time, and electrode potential value, among others. A scanning electron microscope (SEM) and an electron density imaging (EDX) technique were used to examine the morphology of the films that were deposited [37,38].

2. Experimental

The samples used in the anodizing procedure were made from pure aluminum coupons (99.999 % pure aluminum) given by Helwan Co. for Non-Ferrous Industries FAC63, which measured 2 cm^2 cm 0.01 cm in size. The samples were physically cleaned using 600-1000m diamond paste type Metadi-USA to remove any surface irregularities and scratches [39, 40]. This was done to remove any surface imperfections and scratches on the surface of the samples. It was decided to employ the chemical polishing technique as a pretreatment step because it was more easily available, easier, safer, and quicker than electropolishing, and it was a feasible alternative to electropolishing.

The effects of anodizing voltages and current densities on the conscience of nonporous and porous anodic alumina anodized in Oxalic and Sulfuric Acids were studied in this study, as well as the results of other studies. Chemical polishing was used to regulate surface roughness on the samples, which were polished for 5 minutes in a 1:14 solution of perchloric acid and ethanol for a total of 15 minutes. Following that, a second washing with pure ethanol and then distilled water are carried out on the samples. Pure aluminum samples were potentiostatically anodized at 2 volts in H_3PO_4 acid solutions for 20 minutes at 25 ^{o}C and 100 revolutions per minute under mechanical stirring conditions. Phosphoric acid concentrations of 20 and 30 % (by volume) were used to electrochemically anodize the aluminum anode and platinum cathode, which had a combined surface area of 1 cm^2 and were immersed in phosphoric acid at concentrations of 20 and 30 % (by volume).

This experiment used two electrodes linked to the +Ve and -Ve poles of a computer-controlled potentiostat (Volta-lab 21) PGP 201 potentiostat, Galvanosatate 20V, 1A with a general generator (France), with the findings being recorded. Following the anodizing technique, the aluminum was exposed for 30 minutes to a chemical solution containing 5 wt. % H_3PO_4 to open the pores in the metal. The surface microstructures of anodized samples (nPAA) and energy dispersive x-ray analysis (EDX) were explored using a Scanning Electron Microscope SEM (JEOL SEM Model 5040) equipped with field emission analysis capabilities.

The sizes of the pores, as well as cross-sectional images, were measured using a scanning electron microscope (SEM) of type ULTRA55 Zeiss field emission, which was used for the experiment. As a cathode, a platinum sheet served as the anode (1 cm^2), and as a reference electrode, a silver/silver chloride (Ag/AgCl) reference electrode served as the cathode (HANNA Instruments, Italy). 0.1 M $Zn(NO_3)_2$ and 0.05 KNO_3 solutions are used in combination with one another as electrodeposition electrolyte solutions for electrodeposition. The resulting film was completely cleaned with bi-distilled water and ethyl alcohol after it had been electrodeposited, and it was then dried at 80 ^{o}C. We carried out anodization of aluminum, electrodeposition of zinc oxide, and voltammetric tests on aluminum and zinc oxide with the use of a Volta-lab 21) PGP 201 potentiostat and Galvanosatate.

3. Results and discussion

3.1. Effect of Duration time

A series of chronoamperometric curves for Al anodization at chronoamperometric potential 2 V were recorded during anodization duration of 10 min, 20 min, and 30 min for the nPAA template in Fig. 1. The electrolytic solution contained 20 % phosphoric acid and was agitated at a rate of 100 revolutions per minute. Fig. 1a shows that a greater value of anodic current density (35 mAcm^{-2}) at the beginning of the

oxide formation (from 1 to 40 seconds) suggests a lower resistance to pore formation than later in the formation process. A decrease in current density (20 mA cm^{-2}) occurs after 40 to 100 seconds, indicating that the film width is small, and that pore formation has begun.

The development of the hole generation begins after 40 to 100 seconds, indicating that the film width is small, and that pore formation has begun. The barrier-type nPAA film was formed within the first few seconds of the anodization process; the current density decays within a few seconds after the start of the procedure (A and B). The current density rises to its maximum value at this point, and the formation of porous type nPAA films is commenced. After then, it begins to progressively decline again.

Finally, until all the aluminum film has been anodized, a steady current density persists throughout the process (curve A, B, C). At the beginning of the oxide generation process, the transients of curve A and curve B exhibit similar behavior in terms of behavior. As shown in Fig. 1b, the current density is lower (20 mA cm^{-2}) at the start of the oxide production (after 2 seconds), indicating that the pore film has a lower resistance. This is consistent with the lower resistance of the pore film. After then, the process of creating the hole begins in earnest.

The anodization curve (c) differs somewhat from curves A and B in several ways. During the early stages of the oxide development, the current density is smaller (5 mA cm^{-2}), as shown by Fig. 1c. As a result, the expansion of the pore formation begins at a faster rate (2 seconds) than in curves A and B after that. The current density of curve C (5 mA cm^{-2}) is lower than the current density of curves A and B, indicating that the resistance of the created porous film is high, regular, and more ordered in its holes than the resistance of the formed porous film.

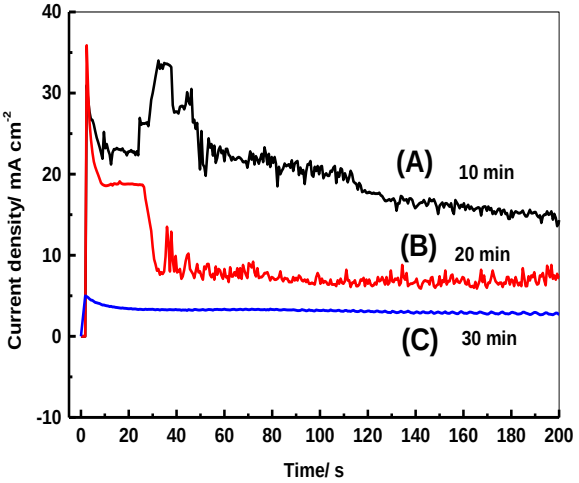

Fig. 1: Anodizing an aluminum sample at 2 V anode potential at 100 rpm at 20% phosphoric acid for 10 minutes, 20 minutes, and 30 minutes results in a typical current transient.

As compared to curves A and B, curve C required less time for nPAA film nucleation and growth for the second anodization, showing that it was more efficient. Consequently, the time it took for curve c to reach a steady-state was shorter than the time it took for curve b to reach the same condition (A and B). Figs. 2a,b,c show SEM pictures that may be used to verify this assertion. Anodization time influences the surface geomorphology of the oxide that forms on a pure aluminum substrate during the anodization process, as seen in the field emission SEM images.

In addition, the hole range predictions may be seen in the SEM photographs. Samples were assessed after being anodized in phosphoric acid concentrations of 10 and 30 % by volume in a phosphoric acid solution, respectively. It was necessary to provide a voltage of 2 V.

Fig. 4a shows the picture of the duration of 30 minutes. A highly uniform nanoporous arrangement with a top view of nearly cylindrical pores of narrow hundreds of nanometers (201, 308 nm) wide, organized structure, was observed. Generally, the oxide layer of Al comprises the barrier layer, which acts as an interlayer between the porous layer and the Al base. The porous layer thickness is higher than the barrier layer. The absence of parallel lines suggests that the anodization of the superficial is started and the corrosion of the hurdle cover has occurred which is followed by a thin, porous film with a nanoporous structure.

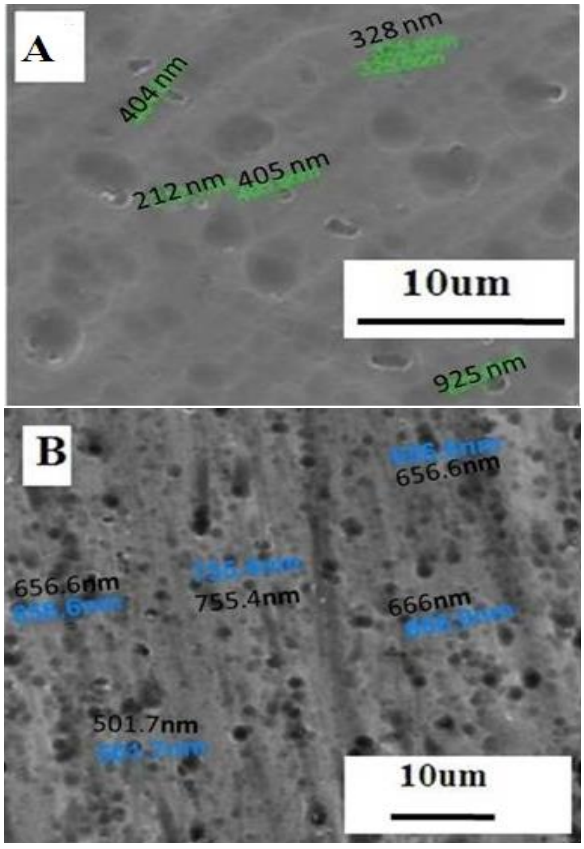

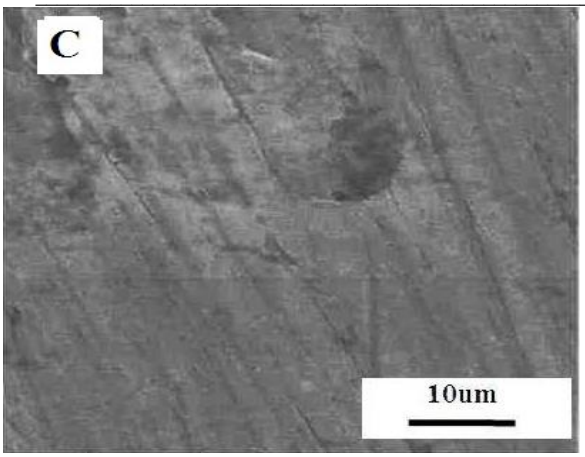

Fig. 2: FESEM images represent the top view of the anodized aluminum surface after electro-anodizing shows the pore size calculations of the initial porous aluminum oxide film formed during first anodization at 20% acid and the anodization is carried out at different periods (a) 30 min, (b) 10 min, (c) Pure Al not anodized.

Fig. 1b shows pictures of the nPAA, which was formed on pure Al substrate in the issue of 20% by duration time 10 minutes. A porous configuration with nearly parallel lines of non-organized porous is shown. Non-uniform porous arrangement along with nearly cylindrical pores of hundreds of nanometers (501, 666 nm) wide structure, was observed. This implies that 10 minutes is not enough for the development of well deep ordered nanoporous layer. SEM image of pure Al substrate is demonstrated in Fig. 2c whereas no anodization was performed.

Fig. 3 shows the chronoamperometric curves for Al anodization at anode potential 2 V in a bath containing 30 % H_3PO_4 with stirred bath at 100 rpm. Fig. 3 shows the chronoamperometric curves for Al anodization at chronoamperometric anodic potential 2 V using 30% phosphoric acid with the same similar conditions. It is noticed from Fig. 3 that, both chronoamperometric curves A and B have an identical behavior at the initiation of the oxide formation (from 1 to 60 seconds) (Curve (a)). This suggests that the progression of the hole creation starts after 2 minutes and represents that, the resulted film is the less porous surface with lower resistance film. After 10 minutes, the decline in the current density (80 mA cm^{-2}) indicates the start of pore formation. Similar behavior is noticed in Fig. 3b.

At the starting of the oxide formation ((from 1 to 60 seconds)) the current density was (60 mA cm^{-2}). This recorded current density value (60 mA cm^{-2}) is lesser than the current of the curve (A) by 20 $mAcm^{-2}$. The evolution of the hole creation is continuous with an increasing anodization time of more than 13 minutes. The current density is highly decreased from 80 to 20 mA cm^{-2} suggests that the development of the regular form of the thin, porous film and represents the establishment of a regular porous film with a steady-state. The anodization curve (c) shows some differences from curves A and B.

Especially in transient behavior. Curve (c) of 30 minutes shows an extremely low current density value (5 mA cm^{-2}) at the starting of the oxide formation. After that, the progression of the hole configuration starts at earlier seconds than curves A and B. Transient of curve C is lower in its current density (5 mA cm^{-2}) value than transient of curves A and B which indicts that the resistance of the created film is high, the pore formed is regular and more ordered in its holes. The time for nPAA nucleation, nPAA film growth, and reaching a steady state was shorter for anodization at 30 minutes curve (c) than curves A and b. This may be confirmed by comparing the SEM images as displayed in 4 A and B.

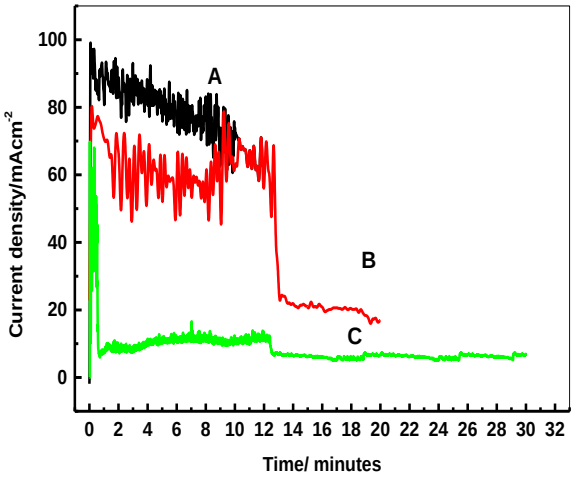

Fig. 3: For various periods (a) 10 minutes (b) 20 minutes (c) 30 minutes, a typical current transient was measured during the anodizing process of Al Sample at anode potential 2 V for 100 rpm in 30 % phosphoric acid

Fig. 4a,b illustrate the consequence of duration time on the SEM pictures of surface morphology for porous anodic Al_2O_3 formed anodized at 30 % acid 10 and 30 minutes. Fig. 4a shows the picture of the duration of 10 minutes. A porous configuration with nearly non-organized porous as demonstrated in image 4.a. Non-uniform porous composition with nearly cylindrical pores of hundreds of nanometers (543, 879 nm) wide structure, was observed. This reveals that 10 minutes is not enough for the development of well deep ordered nanoporous layer.

Alternatively, Fig. 4b shows a more uniform nanoporous composition with acceptable cylindrical pores of narrow hundreds of nanometers (543, 827 nm) wide with an organized structure, which was observed with 30 minutes. The hole configuration becomes more regular and ordered.

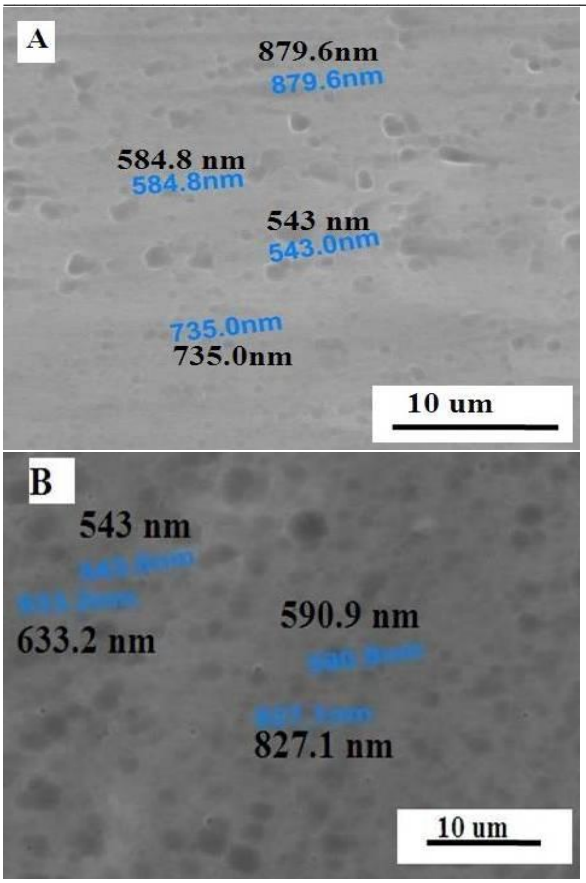

Fig. 4: Electro anodized Al surface with FESEM photos showing the pore size computation at 30 % acid for various periods of exposure (a) 10 minutes of anodization; (b) 30 minutes of anodization.

3.2. Role of Acid concentration

The electrolyte composition largely whether the oxide coating formed is either barrier or porous. Barrier oxides are insoluble in the electrolyte or dissolve at a much slower rate than it is deposited. Furthermore, the impediment coat tends to grow in absence of acid and form an amorphous protective layer over the surface of the Al electrode. The influence of acid load on one-step anodization is displayed in Fig. 5. The nPAA films were formed using one-step anodization in 20 and 30% phosphoric acid using chronoamperometric mode (2 Volt). During the first time of the anodization process, curve (B) of 30% acid shows a higher current density (70 $mAcm^{-2}$) value than 5 mA cm^{-2} of the curve (A).

The barrier-type nPAA film was grown; after that, while porous-type nPAA film growth was initiated, the current density increases to reach a maximum value (curve B, 70 $mAcm^{-2}$) and (curve A, 5 mA cm^{-2}). Subsequently, it slightly decreases again. Finally, a steady current density continues while waiting for all Al layers to be entirely anodized (Curve A and B). Curve (a) of 20% acid shows a lower current density value (5 mA cm^{-2}) at the opening of the oxide formation. After that, the increase of the hole creation starts at earlier seconds (2 seconds) than curve B of 30% acid.

Transient of curve A is lower in its current density (5 mA cm^{-2}) value than transient of curve B (30% acid) which indicts that the resistance of the created film is high. The chronoamperometric behavior of curve (A) signifies that the pore formed is regular and more ordered in its holes. The lower current density of the transient represents higher film resistance. The time for nPAA nucleation and nPAA film development for the second anodization of curve A was shorter than the first anodization of curve B.

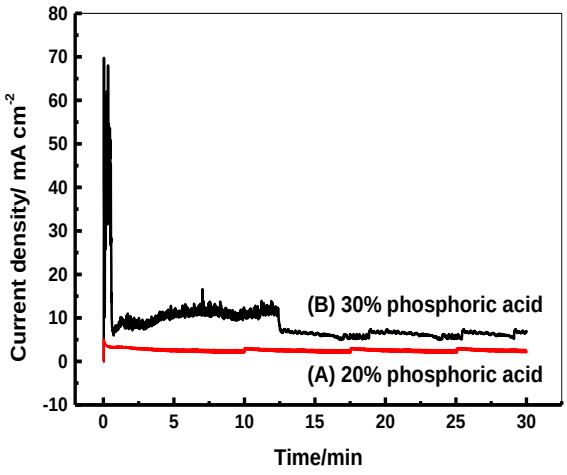

Fig. 5: Recorded during anodizing of Al sample at 2 V anode chronoamperemetric potential and 100 rpm at 20% and 30% phosphoric acid solution concentrations for 30 minutes at anode chronoamperemetric potential 2 V.

Therefore, the period for reaching a steady-state was then shortened for anodization at 20% acid concentration. The resistance of the established PAA film using 20% acid is higher than that of 30% acid samples. Also, the weight loss of 20 % acid sample is higher than samples of 30% acid and the formed layer of nanoporous samples is thinner than samples of 30% acid. Field emission SEM images in Fig. 6a,b illustrate the influence of acid loads on the superficial geomorphology of porous anodic Al_2O_3 formed on pure Al substrate. Specimens were tested after anodizing in 20 and 30 % by volume H_3PO_4. The applied voltage was 2 V with a duration of 30 minutes.

Fig. 2a shows an impression of the nPAA which was formed in the argument of 20% by volume acid. A highly uniform porous configuration with nearly ordered pores of hundreds of nanometers (201, 308 nm) wide, organized in an almost hexagonal structure, was observed. Fig. 2b shows an impression of the nPAA which was formed in the argument of 30% by volume acid. A slightly uniform porous composition with near pores of wider hundreds of

nanometers (543,590 nm) wide, organized in an almost less ordered structure, was observed.

Generally, the oxide cover of Al comprises the barrier layer, which acts as an interlayer between the porous layer and the Al base. The porous layer thickness is higher than the barrier layer. The cell structure surrounding the pore is composed of randomly oriented crystallites. From Fig. 3b the measure pore size formed on pure Al substrate was 113-386nm.

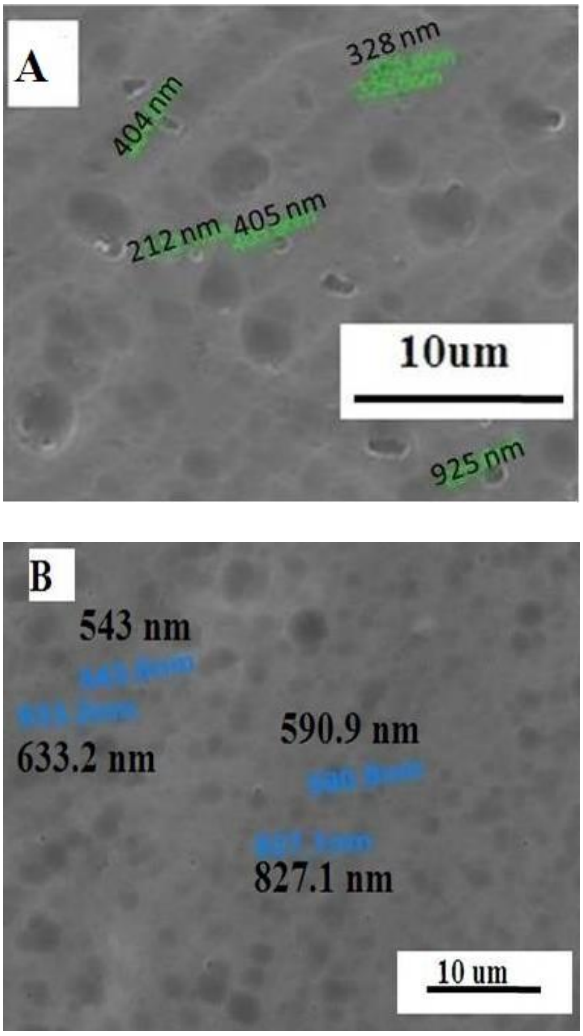

Fig. 6: The pore size estimates generated on Al substrate at chronoamperometric 2 V and 30 min at various acid concentrations (a) 20% (b) 30% are shown in FESEM images for top view in (nPAA).

3.3. ZnO deposition using cyclic voltammetry studies.

3.3.1. Consequence of anodization time: -

ZnO nanowire arrays have also been synthesized by one-step electrodeposition based on nPAA templates conducted in aqueous zinc nitrate solutions [20]. Al Samples are electro anodized in 20% phosphoric acid for different times (10-40 minutes) and followed by one-step ZnO deposition in its nanoporous alumina. In Fig. 7a we compare the electrochemical behavior of ZnO voltammogram with anodized and not anodized Al samples (CV 1, CV 2). Fig. 7a displays the cyclic voltammograms recorded in the deposition blend of 0.1 M Zn $(NO_3)_2$ + 0.05 M KNO3 for anodized and non-anodized Al samples.

For non-anodized samples, CV1 confirms that the cathodic deposition current begins at -1.2 V (Ag/AgCl) recording an extremely low current value -2 mA cm^{-2}. At the cathode potential of -1.2 V, vertical growth of the cathodic current takes place up to -10 mA cm^{-2} corresponding to low ZnO deposition on the minimal cover zone (non-porous) Al substrate [21]. For the anodized Al sample, CV2 the Al sample is electro anodized in 20% phosphoric acid for 30 minutes, followed by ZnO deposition in its porous Al_2O_3. The recorded voltammogram CV2 verifies that the cathodic deposition of a current starts at -0.9 V recording the current value of -10 mA cm^{-2}. At the cathode potential of -1.2 V, a steep escalation of the cathodic current takes place up to -55 mA cm^{-2} corresponding to a high rate of ZnO deposition on high surface area (porous) Al substrate. For both voltammograms (Fig. 7a CV1, CV2), the zinc dissolution peak during the anodic reversing direction is absent in the nitrate bath, suggesting that the route of formation of metallic zinc does not occur using zinc nitrate solution. Experimental observations from CV studies (Fig. 7a) reveal that a potential window between -0.8 and -1.2 V (Ag/AgCl) is suitable for the formation of ZnO films. Fig. 7b displays the cyclic voltammograms recorded with ZnO deposition on nPAA templates. Al samples are electro anodized in 20% phosphoric acid for different durations (10-40 minutes), followed by one-step ZnO deposition in its nPAA.

It is noticeable that during the negative-going scan a cathodic peak is observed at approximately -0.9 V and can be attributed to the metallic zinc oxide deposition for 4 voltammograms. As the potential goes to a more negative value (more than -1V), a diminution in the cathodic current can be detected since the nPAA electrode is covered by ZnO, and it behaves now as a ZnO electrode with different catalytic activity compared to the nPAA electrode. After -1.4 V, the cathodic current escalations again due to the decline of water molecules. The current density of ZnO deposition for 4 voltammograms (CV1, CV2, CV3, CV4) increases gradually with anodization time and attained a supreme value of -55 mA cm^{-2} for 30 minutes sample which designates a high deposition reaction proportion of ZnO on this nPAA porous sample and high growth rate within this high surface area. Alternatively, with the growth of anodization time to 40 minutes, the cathodic current of the ZnO deposition voltammogram (CV4) decreases significantly to -45 mA cm^{-2}. This may be caused by the probability that, the Al template with of 40 mints

was totally dissolved and had been thoroughly eroded or failed so that a too low growth ratio of ZnO was observed. Excess anodized duration also harms nPAA quality [43, 44].

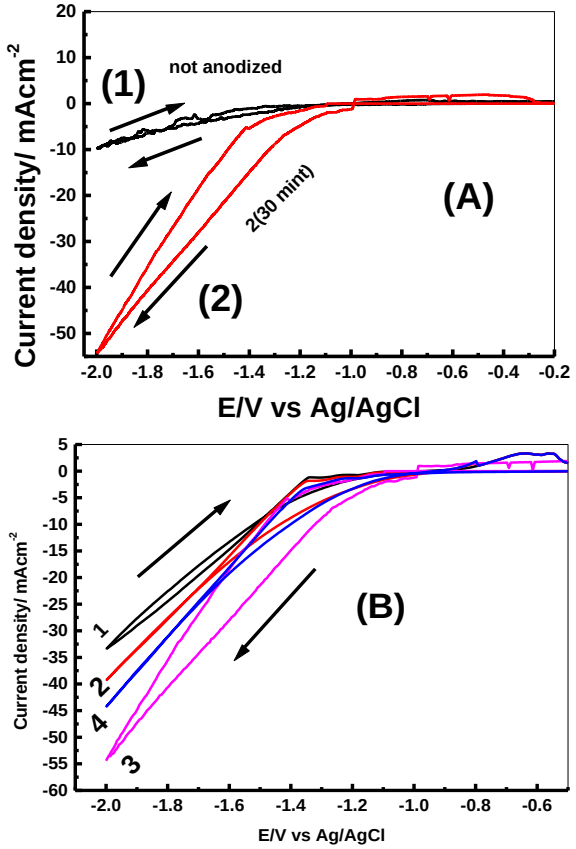

Fig. 7: Voltammograms of ZnO deposition on porous aluminum anodized for 30 minutes and non-porous aluminum anodized for 20 % phosphoric acid are shown in (A).

Voltammograms of ZnO deposition on nanoporous Al cathode anodized in 20% phosphoric acid for (1) 10 min, (2) 20 min, (3) 30 min, (4) 40 min are shown in (B).

3.4. ZnO deposition Stirring effect LSV curve.

3.4.1. LSV rpm effect

ZnO dep on porous Al_2O_3, 20 ml 0.1 M $Zn(NO_3)_2$ + 20 ml 0.05M KNO_3, Anodized porous Alumina cathode 1 cm^2 20% phosphoric acid for 30 mint Ag/AgCl, Pt anode 1cm^2, 10mVs, 25C.

3.4.2. Influence of agitation

Fig. 8 demonstrates the linear sweep voltammetric curves recorded at various agitation rates in a 0.05 M $Zn(NO_3)_2$ and 0.05M KNO_3 solution. Al samples are electro anodized in 20% phosphoric acid for 30 minutes followed by one-step ZnO deposition in its nanoporous Al_2O_3. The curve demonstrates that the cathodic current of ZnO deposition increases with increasing agitation rates from 0 to 1400 rpm. The thickness of the neighboring cathodic layer is reduced when the solution agitation rate is increased, which shortens the diffusion route of ZnO deposition inside the nPAA substrate.

The thin film of electrodeposition of ZnO from concentrated $Zn(NO_3)_2$ baths is constrained by the sluggish kinetics of charge transfer and the mass transfer limitation of the current with dilute concentrations. Although the results show that the greatest increase in current density towards a more negative value is combined with the upsurge in agitation rate from 0 rpm to 1000 rpm, the deposited film resulting at 0 rpm is more compact and homogenous. With the growth of the speed of agitation to 200 rpm, the deposit becomes poor and uncovered areas of the surface are observed. At a high agitation rate, 1000 rpm, the film is likely depleted or damaged which is generated from a bad quality cathode deposit. Therefore, the production of the ZnO film in a stagnant solution (0 rpm), in the current study, is advantageous for obtaining a better film quality.

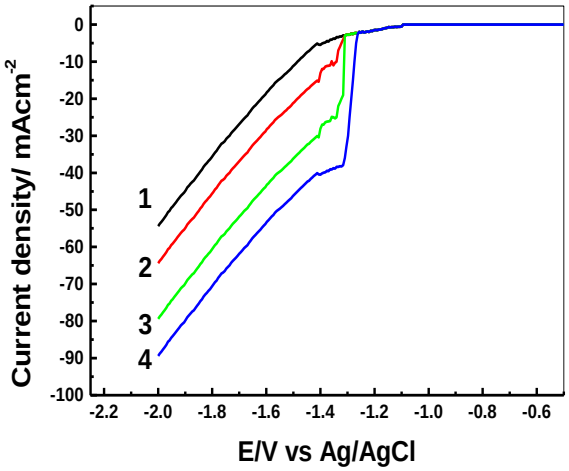

Fig. 8: NPAA cathode in Zn(NO3)2+0.05 M KNO3 solution was used to measure linear sweep voltages at agitation speeds as low as zero and as high as 500 revolutions per minute (rpm) in 0.1 M $Zn(NO_3)_2$ + 0.05 M KNO_3. It takes 10 mV-1 to sweep the potential. The current temperature is a balmy ^0C.

3.4.3. Potentiostatic deposition ZnO

Fig. 9 displays the chronoamperometric curves recorded with nPAA substrate in the deposition medium of 0.1 M Zn $(NO_3)_2$ and 0.05 M KNO_3. All nPAA samples are anodized at 20% acid for 30 minutes with stirred bath. The data shows the corresponding current density behaviors from the potentials -0.9, -1 and -1.2 V applied to the electrode arrangement of nanostructured ZnO with identical electrodeposition periods (600 s).

Three distinct transients were detected for the three tested potentials, -0.9, -1 and 1.2 V. Immediately after potential application, the cathodic current rapidly increases because the nucleation starts, and the three-dimensional growth of each crystal rapidly increases the active surface area. Generally, the inflection point around 80 s indicates the transient from nanotubes to

nanorods that, steady-state of the transient with time up to 600 s as a result of complete nanorods formations. At lower potential (-0.9 V) the corresponding current stabilized after a slight current drop, maintaining a relatively smaller current drop (-1.25 $mAcm^{-2}$), as signaled in Fig. 9a. This result implies that the nucleation of ZnO takes place at numerous sites in the holes and then deposited small grains from along layer walls. The shape is typical of the electro-crystallization growth process for the three tested potentials.

The current tosses through a maximum during the coalescence process curve (a-c). The emergence of the peak when potential increases can be attributed to a higher density of nucleation sites as confirmed from SEM views. Further increase in deposition period (100 to 600 s) causes a reduction in the current density to a constant plateau value.

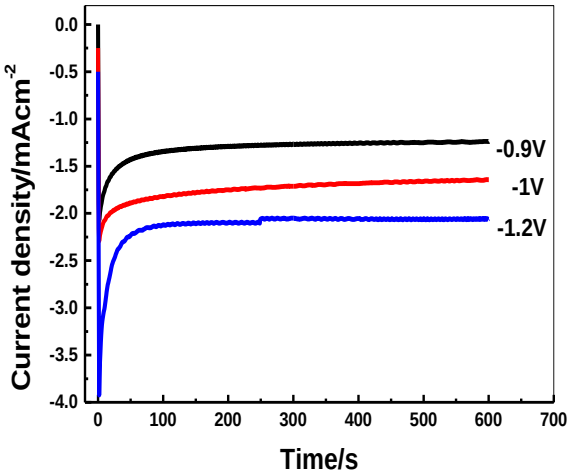

Fig.9: Curves obtained with a nPAA substrate in an aqueous solution of $Zn(NO_3)_2$ + 0.05 M KNO_3 at -0.9,-1,-1.2 v/Ag/AgCl potentials.

This may be confirmed by the SEM picture and EDX indicated in Fig. 10a for -0.9 V. At relatively higher potential (-1 V) the corresponding current stabilized after a slight current drop, maintaining a relatively high current drop (-1 $mAcm^{-2}$), as shown in Fig. 10b. At higher potential (-1.2 V) the corresponding current stabilized after a slight current drop, maintaining a relatively high current drop (-2.25 $mAcm^{-2}$), and indicating a high deposition rate. At a potential of -1.2 V, ZnO nanowires are uniform and smoother than that of ZnO deposited at -0.9 V. Deposition ratio of ZnO with -1.2 V is higher than with -0.9 V, as seen in (EDX study Fig. 10b). High cathodic deposition current transient (-2.25 mA cm^{-2}) is observed with -1.2 V. The rate of ZnO deposition is higher than -0.9 V. This may be confirmed by comparing the SEM images and EDX shown in Fig. 10a,b. Fig. 10b shows the SEM pictures of the underside of the ZnO nanowires on nPAA. Bright regions show nanowires with filled pores and dark regions show unfilled pores. Fig. 10 (-0.9 V) shows the surface image of ZnO nanowires with the nPAA template partly filled. Fig. 10b also shows the EDX spectra obtained for ZnO film deposited at -0.9 V and -1.2 V on nPAA for 600 s. The ZnO was deposited from a bath containing 0.1 $Zn(NO_3)_2$+0.05M KNO_3. EDX data reveals that the elemental percentage of Zn and oxygen are 9.62 and 1.36 for ZnO deposited at potential -1.2 V (Fig. 10b). In contrast, the elemental percentage of Zn and oxygen are 1.96 and 3.67 for ZnO deposited at a potential -0.9 V (Fig. 10a). The deposition ratio of ZnO as seen is high with -1.2 V than -0.9 V. High cathodic deposition current transient is observed with -1.2 V. The ratio of ZnO deposition is higher than -0.9 V [45].

3.5. Characterization of synthesized ZnO/Al_2O_3

The surface layer of the created samples was examined using scanning electron microscopy (SEM), and the chemical composition of the surface layer was examined using energy-dispersive X-ray spectroscopy (EDXS) to determine its chemical composition (EDX) [46]. The results of the research demonstrated that the structural arrays of nanowires employed in the studies were of good quality. According to the images supplied, the ZnO nanowires have grown uniformly and evenly across the lowest region of the structure, including the space between the nanowires, according to the photographs provided [47]. The length of the ZnO nanowires was reported to be around 500 nanometers, while the diameter of the wires was revealed to be between 30 and 50 nanometers. Based on the images, it can be observed that the surface is smooth, which is supported by superb crystallization and crystal orientation that is uniform throughout the sample [48, 49]. By increasing smoothness, electronic conduction is improved, which in turn improves the photocatalytic activity of the material. (See Fig. 1).

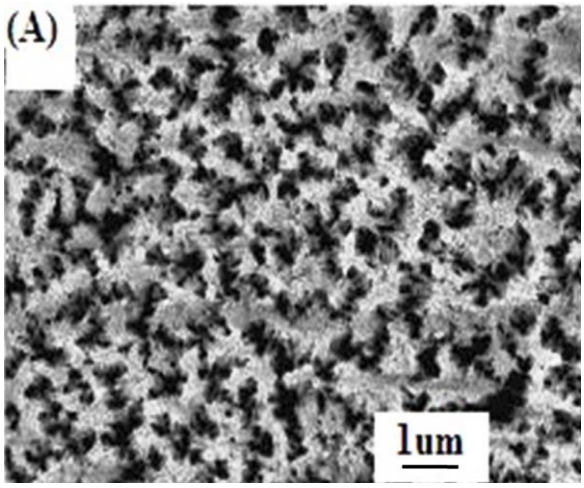

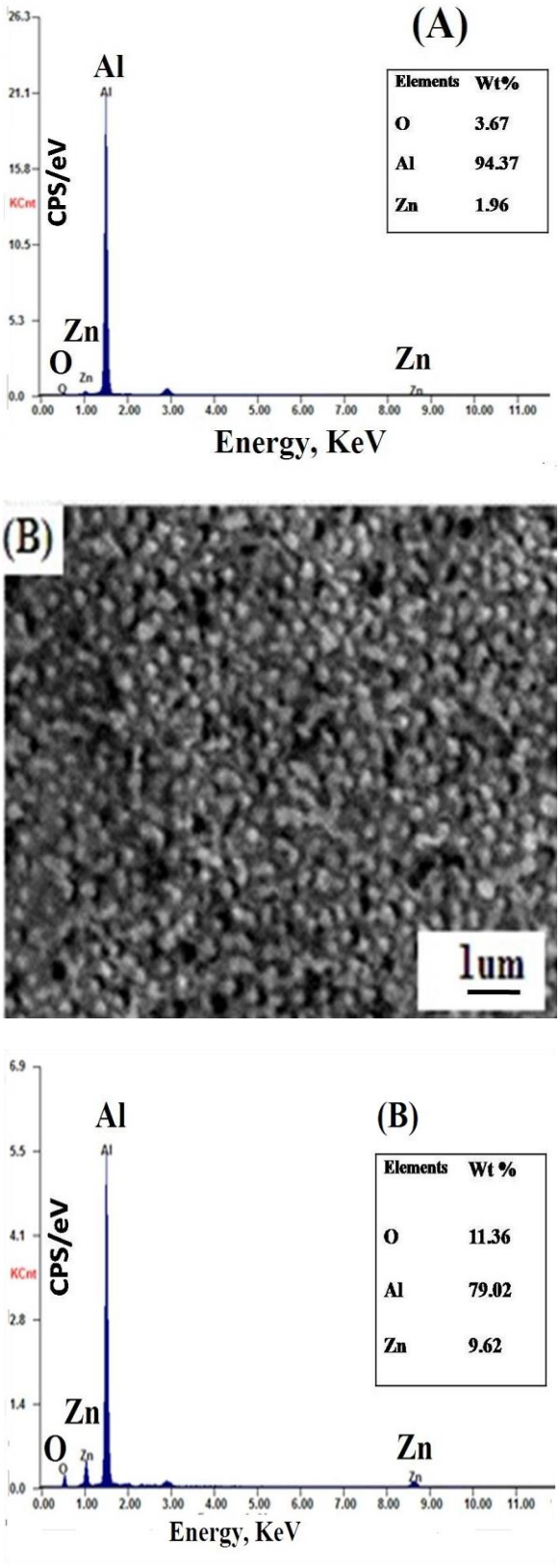

Fig 10: (A and b) FESEM pictures and EDX spectra at potentials (a) -0.9 V (b) -1.2 V for 11 minutes illustrate the deposition of ZnO nanowire within an nPAA template.

4. Conclusion

nPAA generated by electrochemical anodization of commercial aluminum will be discussed on this page concerning the acid load applied to the anode. The morphology of the PAA was categorized using the following criteria: (SEM). The electrochemical deposition of nanowire ZnO on nanoporous alumina was also discussed at the meeting (nPAA). Also investigated and addressed where the impacts of anodization time, deposition potential, and stirring rate on the development of ZnO on nPAA, among other things.

All the integrated experiments were categorized based on their use of EDX, or field emission scanning electron microscopy, as their primary imaging technique (FESEM). Given the bulky superficial zone, which has the greatest effect on improving catalytic performance, the results given revealed that ZnO nanotubes were able to absorb more light, resulting in an increased photolysis efficiency, which was proved by the data presented. This means that these nanowires and the features connected with them have the potential to be employed in photocatalysis, as well as other fields like solar energy and a range of sensor applications.

Declaration of Competing Interest

The authors declare that they have no known competing financial interests or personal relationships that could have appeared to influence the work reported in this paper.

Acknowledgments

Not available

References

[1] Qiu Y., Yan K., Deng H., Yang S. Secondary branching, and nitrogen doping of ZnO nano tetrapods: building a highly active network for photoelectrochemical water splitting Nano Lett., 12: 407–413 (2012).

[2] Zhou H., Feng M., Feng M., Gong X., Zhang D., Zhou Y., Chen S. Gradient doping of sulfur in Sb_2Se_3 nanowire arrays as photoelectrochemical photocathode with a 2% half-cell solar-to-hydrogen conversion efficiency Appl. Phys. Lett., 116: 113902 (2020).

[3] Wang K., Huang D., Yu L., Feng K., Li L., Harada T., Ikeda S., Jiang F. Promising GeSe nanosheet-based thin-film photocathode for efficient and stable overall solar water splitting ACS Catal., 9: 3090–3097 (2019).

[4] Li Z., Liang X., Li G., Liu H., Zhang H., Guo J., Chen J., Shen K., San X., Yu W., Schropp R.E. I., Mai Y. 9.2%-efficient core-shell structured antimony selenide nanorod array solar cells Nat. Commun., 10: 125 (2019).

[5] Zhang L., Li Y., Li C., Chen Q., Zhen Z., Jiang X., Zhong M., Zhang F., Zhu H. Scalable low-band-Gap Sb_2Se_3 thin-film photocathodes for efficient

visible-near-infrared solar hydrogen evolution ACS Nano, 11: 12753–12763 (2017).
[6] Yue X., Yi S., Wang R., Zhang Z., Qiu S. Synergistic effect based NixCo1-x architected Zn0.75Cd0.25S nanocrystals: an ultrahigh and stable photocatalyst for hydrogen evolution from water splitting Appl. Catal., B224: 17–26 (2018).
[7] Zhou H., Feng M., Song K., Liao B., Wang Y., Liu R., Gong X., Zhang D., Cao L., Chen S. A highly [001]-textured Sb_2Se_3 photocathode for efficient photoelectrochemical water reduction Nanoscale, 11: 22871–22879 (2019).
[8] Zhou X., Wang X., Feng X., Zhang K., Peng X., Wang H., Liu C., Han Y., Wang H., Li Q. Loading Cd0.5Zn0.5S quantum dots onto onion-like carbon nanoparticles to boost photocatalytic hydrogen generation ACS Appl. Mater. Interfaces, 9: 22560–22567 (2017).
[9] Zohdy K. M., El-Sherif R. M., El-Shamy A. M. Corrosion and Passivation Behaviors of Tin in Aqueous Solutions of Different pH J of Bio-and Tribo-Corrosion, 7(2): 1-7 (2021).
[10] Guo L., Shinde P.S., Ma Y., Li L., Pan S., Yan F. Scalable core-shell MoS_2/Sb_2Se_3 nanorod array photocathodes for enhanced photoelectrochemical water splitting Sol. Rrl, 4: 1900442 (2020).
[11] El-Shamy A. M., Abdel Bar M. M. Ionic Liquid as Water Soluble and Potential Inhibitor for Corrosion and Microbial Corrosion for Iron Artifacts Egyptian Journal of Chemistry, 64(4): 1867-1876 (2021).
[12] Zhou H., Feng M., Feng M., Gong X., Zhang D., Zhou Y., Chen S. Gradient doping of sulfur in Sb_2Se_3 nanowire arrays as photoelectrochemical photocathode with a 2% half-cell solar-to-hydrogen conversion efficiency Appl. Phys. Lett., 116: 113902 (2020).
[13] Zohdy K. M., El-Sherif R. M., Ramkumar S., El-Shamy A. M., Quantum and electrochemical studies of the hydrogen evolution findings in corrosion reactions of mild steel in acidic medium Upstream Oil and Gas Technology, 6: 100025 (2021).
[14] Qiu Y., Yan K., Deng H., Yang S. Secondary branching and nitrogen doping of ZnO nanotetrapods: building a highly active network for photoelectrochemical water splitting Nano Lett., 12: 407–413 (2012).
[15] Reda Y., El-Shamy A. M., Zohdy K. M., Eessaa A.K. Instrument of chloride ions on the pitting corrosion of electroplated steel alloy 4130, Ain Shams Engineering Journal, 11(1): 191-199 (2020).
[16] Wang J., Kuo M., Zeng P., Xu L., Chen S., Peng T. Few-layer $BiVO_4$ nanosheets decorated with $SrTiO_3$: Rh nanoparticles for highly efficient visible-light-driven overall water splitting, Appl. Catal., B279: 119377 (2020).
[17] Reda Y., Zohdy K. M., Eessaa A. K., El-Shamy A. M. Effect of Plating Materials on the Corrosion Properties of Steel Alloy 4130, Egyptian Journal of Chemistry, 63(2): 579-597 (2020).
[18] Reda Y., El-Shamy A. M., Eessaa A. K. Effect of hydrogen embrittlement on the microstructures of electroplated steel alloy 4130, Ain Shams Engineering Journal, 9 (4): 2973-2982 (2018).
[19] Zhang Y., Zhang Y., Guo W., Johnston-Peck A.C., Hu Y., Song X., Wei W.D. Modulating multi-hole reaction pathways for photoelectrochemical water oxidation on gold nano catalysts, Energy Environ. Sci., 13: 1501–1508 (2020).
[20] Eessaa A. K., El-Shamy A. M. Reda Y. Fabrication of Commercial Nanoporous Alumina by Low Voltage, Egyptian Journal of Chemistry, 61(1): 175-185 (2018).
[21] Gao J., Sahli F., Liu C., Ren D., Guo X., Werner J., Jeangros Q., Zakeeruddin S.M., Ballif C., Gr¨atzel M., Luo J. Solar water splitting with perovskite/silicon tandem cell and TiC supported Pt nanocluster electrocatalyst, Joule 3: 2930–2941 (2019).
[22] Farag H. K., El-Shamy A. M., Sherif E. M., El Abedin S. Z. Sonochemical Synthesis of Nanostructured ZnO/Ag Composites in an Ionic Liquid, Zeitschrift für Physikalische Chemie, 230(12): 1733-1744 (2016).
[23] Kim J., Yang W., Oh Y., Lee H., Lee S., Shin H., Kim J., Moon J. Self-oriented Sb_2Se_3 nanoneedle photocathodes for water splitting obtained by a simple spin-coating method, J. Mater. Chem., A5: 2180–2187 (2017).
[24] Yang W., Lee S., H. Kwon C., Tan J., Lee H., Park J., Oh Y., Choi H., Moon J., Time-resolved observations of photo-generated charge-carrier dynamics in Sb_2Se_3 photocathodes for photoelectrochemical water splitting ACS Nano, 12: 11088–11097 (2018).
[25] Wang Z., Qi Z., Fan X., Leung D.Y.C., Long J., Zhang Z., Miao T., Meng S., Chen S., Fu X., Intimately contacted Ni_2P on CdS Nanorods for highly efficient photocatalytic H_2 evolution: new phosphidation route and the interfacial separation mechanism of charge carriers, Appl. Catal., B281: 119443 (2021).
[26] Kosco J., Bidwell M., Cha H., Martin T., Howells C.T., Sachs M., Anjum D.H., Gonzalez S. Lopez, Zou L., Wadsworth A., Zhang W., Zhang L., Tellam J., Sougrat R., Laquai F., DeLongchamp D.M., Durrant J.R., McCulloch I. Enhanced photocatalytic hydrogen evolution from organic semiconductor heterojunction nanoparticles Nat. Mater., 19: 559–565 (2020).
[27] Wang K., Xing Z., Meng D., Zhang S., Li Z., Pan K., Zhou W. Hollow MoSe2@Bi2S3/ CdS core-shell nanostructure as dual Z-Scheme

heterojunctions with enhanced full spectrum photocatalytic-photothermal performance Appl. Catal., B281: 119482 (2021).
[28] Xiao M., Wang Z., Lyu M., Luo B., Wang S., Liu G., Cheng H. M., Wang L. Hollow nanostructures for photocatalysis: advantages and challenges Adv. Mater., 31: 1801369 (2019).
[29] Yao L., Wang W., Zhu T., Wang Y., Liang Y., Fu J., Wang J., Cheng Y., Liu S. A rational design of $CdS/ZnFe_2O_4/Cu_2O$ core-shell nanorod array photoanode with stair-like type-II band alignment for highly efficient bias-free visible-light-driven H_2 generation Appl. Catal., B268: 118460 (2020).
[30] Tan J., Yang W., Oh Y., Lee H., Park J., Boppella R., Kim J., Moon J. Fullerene as a photoelectron transfer promoter enabling stable TiO_2-protected Sb_2Se_3 photocathodes for photo-electrochemical water splitting Adv. Energy Mater., 9: 1900179 (2019).
[31] Wick-Joliat R., Musso T., Prabhakar R.R., L¨ockinger J., Siol S., Cui W., S´every L., Moehl T., Suh J., Hutter J., Iannuzzi M., Tilley S.D. Stable and tunable phosphonic acid dipole layer for band edge engineering of photoelectrochemical and photovoltaic heterojunction devices Energy Environ. Sci., 12: 1901–1909 (2019).
[32] Lee H., Yang W., Tan J., Oh Y., Park J., Moon J. Cu-doped NiOx as an effective holeselective layer for a high-performance Sb_2Se_3 photocathode for photoelectrochemical water splitting ACS Energy Lett., 4: 995–1003 (2019).
[33] Li R., Xie Z., Lu H., Zhang D.W., Yu A. Fabrication of $ZnO@TiO_2$core–shell nanotube arrays as three-dimensional anode material for lithium-ion batteries Int. J. Electrochem. Sci., 8: 11118–11124 (2013).
[34] Martinson A.B.F., Elam J.W., Hupp J.T., Pellin M.J. ZnO nanotube-based dye-sensitized solar cells Nano Lett., 7 (2007) 2183–2187.
[35] Yang C.J., Wang S.M., Liang S.W., Chang Y.H., Chen C., Shieh J.M. Low-temperature growth of ZnO nanorods in anodic aluminum oxide on Si substrate by atomic layer deposition Appl. Phys. Lett., 90: 033104 (2007).
[36] Chang Y.H., Wang S.M., Liu C.M., Chen C. Fabrication and characteristics of self-aligned ZnO nanotube and nanorod arrays on Si substrates by atomic layer deposition J. Electrochem. Soc., 157: K236 (2010).
[37] Li X.L., Li C., Zhang Y., Chu D.P., Milne W.I., Fan H.J. Atomic layer deposition of ZnO on multi-walled carbon nanotubes and its use for the synthesis of CNT-ZnO heterostructures Nanoscale Res. Lett., 5: 1836–1840 (2010).
[38] Pietruszka R., Witkowski B.S., Luka G., Wachnicki L., Gieraltowska S., Kopalko K., Zielony E., Bieganski P., Placzek-Popko E., Godlewski M. Photovoltaic properties of ZnO nanorods/p-type Si heterojunctionstructures Beilstein J. Nanotechnol., 5: 173–179 (2014).
[39] Edley M.E., Li S., Guglietta G.W., Majidi H., Baxter J.B. Ultrafast charge carrier dynamics in extremely thin absorber (ETA) solar cells consisting of CdSe-coated ZnO nanowires J. Phys. Chem., C 120: 19504–19512 (2016).
[40] Yuan K., Cao Q., Li X., Chen H.Y., Deng Y., Wang Y.Y., Luo W., Lu H.L., Zhang D.W. Synthesis of $WO_3@ZnWO_4@ZnO$–ZnO hierarchical nano cactus arrays for efficient photoelectrochemical water splitting Nano Energy, 41: 543–551 (2017).
[41 Jeong] J.S., Choe B.H., Lee J.H., Lee J.J., Choi W.Y. ZnO-coated TiO_2nanotube arrays for a photoelectrode in dye-sensitized solar cells J. Electron. Mater., 43: 375–380 (2014).
[42] Cai H., Yang Q., Hu Z., Duan Z., You Q., Sun J., Xu N., Wu J. Enhanced photoelectrochemical activity of vertically aligned ZnO-coated TiO_2nanotubes Appl. Phys. Lett., 104: 053114 (2014).
[43] Cai H., You Q., Hu Z., Duan Z., Cui Y., Sun J., Xu N., Wu J. Fabrication, and correlation between photoluminescence and photoelectrochemical properties of vertically aligned ZnO coated TiO_2 nanotube arrays, Sol. Energy Mater. Sol. Cells, 123: 233–238 (2014).
[44] Zeng M., Zeng X., Peng X., Zhu Z., Liao J., Liu K., Wang G., Lin S. Improving photoelectrochemical performance on quantum dots co-sensitized TiO_2 nanotube arrays using ZnO energy barrier by atomic layer deposition Applied Surface Science, 388: 352–358 (2016).
[45] Cai H., Liang P., Hu Z., Shi L., Yang X., Sun J., Xu N., Wu J. Enhanced photoelectrochemical activity of ZnO-coated TiO_2nanotubes and its dependence on ZnO coating thickness Nanoscale Res. Lett. ,11: 1–11 (2016).
[46] Amal M. Abdel‑ Karim, Ashraf M. El‑ Shamy, A Review on Green Corrosion Inhibitors for Protection of Archeological Metal Artifacts, Journal of Bio- and Tribo-Corrosion 8: 35 (2022).
[47] A. M. El-Shamy, M. A. El-Hadek, A. E. Nassef, R. A. El-Bindary, Optimization of the influencing variables on the corrosion property of steel alloy 4130 in 3.5 wt.% NaCl solution, Journal of Chemistry 2020: Article ID 9212491.
[48] A. M. El-Shamy, A Review on: Biocidal Activity of Some Chemical Structures and Their Role in Mitigation of Microbial Corrosion, Egyptian Journal of Chemistry, 63(12): 5251-5267 (2020).
[49] Y. Reda, H. M.Yehia, A. M.El-Shamy, Microstructural and mechanical properties of Al-Zn alloy 7075 during RRA and triple aging, Egyptian Journal of Petroleum 31: 9–13 (2022).